New Aspects of Energy Conversion in Magnetic Island Dynamics: Particle-in-cell Simulation of Multiple Island Coalescence and MMS Observations

Teh, W.-L.

Nakamura, T. K. M.

Zenitani, S.

Umeda, T.

Nakamura, R.

The Astrophysical Journal, 947:4 (9pp), 2023 April 10 https://doi.org/10.3847/1538-4357/acc2bf

New Aspects of Energy Conversion in Magnetic Island Dynamics: Particle-in-cell Simulation of Multiple Island Coalescence and MMS Observations

W.-L. Teh[1], T. K. M. Nakamura[2,3], S. Zenitani[4], T. Umeda[5], and R. Nakamura[2]
[1] Space Science Centre, Institute of Climate Change, Universiti Kebangsaan Malaysia, Bangi, Malaysia
[2] Space Research Institute, Austrian Academy of Sciences, Graz, Austria
[3] Krimgen LLC, Hiroshima, Japan
[4] Research Center for Urban Safety and Security, Kobe University, Kobe, Japan
[5] Institute for Space-Earth Environmental Research, Nagoya University, Nagoya, Japan
Received 2022 October 31; revised 2023 February 27; accepted 2023 March 7; published 2023 April 11

Abstract

Coalescence of multiple magnetic islands is recognized as an effective process to energize particles during magnetic reconnection, while its energy conversion process still remains unclear. Here, a two-dimensional fully kinetic simulation of multiple island coalescence with a small reconnection guide field is studied. In the analysis of energy conversion within a magnetic island, the dot product of $\boldsymbol{V}_e \cdot (\boldsymbol{j} \times \boldsymbol{B}) = w_1$ is a useful quantity to compare with $\boldsymbol{j} \cdot \boldsymbol{E} = w_2$, since the average work done by the Lorentz force on the circulating particles is negligible in the island and $w_2 - w_1 = \boldsymbol{j} \cdot (\boldsymbol{E} + \boldsymbol{V}_e \times \boldsymbol{B}) = \boldsymbol{j} \cdot \boldsymbol{E}' = w_3$. A bipolar pattern of w_1 is found at a secondary island when the electrons are in circular motion inside the island. Significant energy dynamo ($w_3 < 0$) resulting from $j_\parallel E_\parallel$ is found at the secondary island, which has not been reported before, where the parallel electric field $E_\parallel$ is highly correlated with w_3. Moreover, significant energy dissipation ($w_3 > 0$) due to $\boldsymbol{j}_\perp \cdot \boldsymbol{E}'_\perp$ is seen in the merging region between two coalescing islands. Both types of energy conversions are accompanied by enhancements in $j_\parallel$ and the parallel electron temperature $T_{e\parallel}$. Three ion-scale magnetic islands (FR1, FR2, and FR3) observed by the Magnetospheric Multiscale spacecraft are compared favorably with the simulated signatures of energy dynamo and dissipation of an evolving secondary island. In particular, FR1 displayed a similar energy dynamo signature as that simulated in an early stage of the secondary island. FR2 and FR3 showed a dominant $\boldsymbol{j}_\perp \cdot \boldsymbol{E}'_\perp$ energy conversion similar to that obtained in a later stage of the secondary island.

Unified Astronomy Thesaurus concepts: Interplanetary physics (827)

1. Introduction

Coalescence is a merging process of two magnetic islands or flux ropes, during which a secondary magnetic reconnection occurs at the merging point (e.g., Pritchett 2008; Oka et al. 2010a; Tanaka et al. 2010; Zank et al. 2014; Zhou et al. 2014). The process of multiple island coalescence has drawn attention in the solar-terrestrial physics community because simulation studies have revealed that during the coalescence process, the charged particles can be efficiently accelerated around the X-line (e.g., Hoshino et al. 2001; Hoshino 2005; Oka et al. 2010a; Tanaka et al. 2010) and also around the island (e.g., Drake et al. 2006; Oka et al. 2010a). Thus, the coalescence process can account for the explosive energy release phenomena on the Sun (e.g., Song et al. 2012) and the energetic particles observed in the magnetic islands or flux ropes in the solar wind (e.g., Khabarova et al. 2015; Zhao et al. 2018, 2019) and in Earth's magnetotail (e.g., Chen et al. 2008; Wang et al. 2010; Huang et al. 2012; Lu et al. 2020; Zhong et al. 2020).

As pointed out by Le Roux et al. (2019), the particle acceleration mechanisms for multiple island coalescence can be expressed in terms of guiding center kinetic theory. The accelerations by the motional electric field consist of the curvature drift acceleration (e.g., Drake et al. 2006) and the gradient-B drift acceleration (e.g., Dahlin et al. 2017), while the acceleration by the parallel electric field is the parallel guiding center motion acceleration (e.g., Oka et al. 2010a). From the nonuniform plasma flow perspective, Le Roux et al. (2018) concluded that the accelerations by the motional electric field can be treated as the compression acceleration and the incompressible parallel shear-flow acceleration. The former is due to the increase of the magnetic field strength caused by the magnetic island compression, while the latter is due to the decrease of the magnetic field strength resulting from the magnetic island contraction or merging. Recently, using the newly developed reconstruction technique, Teh (2022a) showed that the pressure anisotropy can change the aspect ratio of the width to the length of the island, for which the pressure anisotropy of $p_\perp > p_\parallel$ can lead to the island contraction (i.e., the decrease in the aspect ratio) while the aspect ratio of the island increases for $p_\parallel > p_\perp$. As a result, the effects of the pressure anisotropy on the geometry of the island would accelerate the particles as those by the nonuniform plasma flow effects.

Small-scale magnetic islands or flux ropes are found to play a key role in particle acceleration (e.g., Zhao et al. 2018, 2019; Lu et al. 2020). These small-scale islands or secondary islands can be generated by the tearing instability in a thinning current sheet (e.g., Daughton et al. 2006; Oka et al. 2010b) and have been observed in the ion and electron diffusion regions of reconnection (e.g., Eastwood et al. 2007; Teh et al. 2010, 2014, 2017, 2018; Teh 2022b; Chen et al. 2021). In situ observations of the multiple island coalescence have been reported in the magnetotail (Wang et al. 2016; Zhao et al. 2016) and the magnetopause (Zhou et al. 2017). One of the main features of the island coalescence is the strong energy

dissipation that occurs in a localized region between two coalescing islands, where $\boldsymbol{j}\cdot(\boldsymbol{E}+\boldsymbol{V}_e\times\boldsymbol{B})=\boldsymbol{j}\cdot\boldsymbol{E}'>0$, indicating the energy conversion from the electromagnetic fields to the particles. The dot product of $\boldsymbol{j}\cdot\boldsymbol{E}'$ is a useful quantity to measure the rate of energy conversion in a tiny region during reconnection (Zenitani et al. 2011). Recently, strong energy dissipation has been reported within a small-scale magnetotail flux rope (Huang et al. 2019), indicating that dynamic energy conversion can occur in the small-scale magnetic flux rope.

This paper aims to examine the energy conversions in the multiple island coalescence using a two-dimensional fully kinetic simulation with a small reconnection guide field ($0.25B_0$). The dot product of $\boldsymbol{V}_e\cdot(\boldsymbol{j}\times\boldsymbol{B})$ is introduced into the analysis of the energy conversion for the island, which is found to be a useful quantity to compare with $\boldsymbol{j}\cdot\boldsymbol{E}$ (Zenitani et al. 2012). Finally, three ion-scale magnetic islands observed by the Magnetospheric Multiscale (MMS) spacecraft are compared with the simulation results.

2. Simulation Model

This simulation was developed to solve the relativistic Vlasov–Maxwell system of equations in 2.5 dimension, using the high-performance particle-in-cell code VPIC (Bowers et al. 2008, 2009). The initial magnetic field components are expressed as $B_x=B_0\tanh(z/L_0)$ and $B_y=B_g$, where B_0 is the background reconnecting magnetic field, B_g is the uniform guide field out of the reconnection plane (i.e., $x-z$ plane), and L_0 is the half-thickness of the initial current sheet. The initial ion and electron number densities are described as $n_{i,e}=n_0\,\mathrm{sech}^2(z/L_0)+n_b$, where n_0 is the Harris-type density, n_b is the background density in the upstream region. The initial density and temperature ratios were set to $n_0/n_b=3.0$, $T_{i0}/T_{e0}=3.0$, $T_{ib}/T_{eb}=3.0$, and $T_{i0}/T_{ib}=T_{e0}/T_{eb}=3.0$, where $T_{i,e0}$ and $T_{i,eb}$ are the Harris-type and background temperatures. These density and temperature ratios were the same as those employed by Nakamura et al. (2018, 2020), based on the MMS observations of multiple magnetic flux ropes in the magnetotail on 2017 July 11 (Stawarz et al. 2018; Teh et al. 2018). The ratio of the electron plasma frequency (ω_{pe}) to the electron gyrofrequency (Ω_e) was 2.0. The guide field $B_g=0.25B_0$ was used, based on the 2017 July 11 reconnection event observed by the MMS spacecraft in the magnetotail (Teh et al. 2018).

The simulation box size was $L_x\times L_z=120\ d_i\times 60\ d_i=2400\ d_e\times 1200\ d_e=14400\times 7200$ cells, with a total of 1.2×10^{11} simulated particles, where d_i and d_e are the ion and electron inertial lengths based on n_0. The ion-to-electron mass ratio was 400. This was a time-consuming PIC simulation, in terms of the number of particles ($>10^{11}$) and mass ratio implemented. The boundary conditions are periodic in x and conducting wall in z. To initiate multiple X-line reconnection, the initial magnetic field perturbations consisted of 16 evenly spaced magnetic islands with a length of $L_x/16=7.5d_i$, which corresponds to the wavelength of the fastest-growing mode of the tearing instability for L_0. The simulation results have also been studied for the spatial and time scaling of coalescing islands and associated plasma heating (Nakamura et al. 2023).

3. Simulation and Observational Results

3.1. Simulation Results

Figures 1(a)–(c) show the magnetic field configuration in the x-z plane at the time $t=90\ \Omega_i^{-1}$, with colors in the axial magnetic field B_y, the axial current density j_y, and the electron density n_e. Here Ω_i is the ion gyrofrequency. There are three large magnetic islands at this time that formed as a result of a gradual coalescence of 16 smaller islands. The two large islands located between $1200d_e<x<2400d_e$ have started to merge. There is also a small secondary magnetic island located at $48d_e<x<144d_e$, which was generated at $t=\sim88\ \Omega_i^{-1}$ due to secondary reconnection in a thinning current sheet. As compared to the ambient density, there is a density increase in both the large islands and the secondary island. The axial current density j_y is large in the secondary and large islands and in the merging region at $x=\sim1690d_e$ as well. The strong j_y in the large islands is mainly located at the regions where the n_e is highly enhanced, as shown by the dark red regions in Figure 1(c).

Figures 1(d)–(g) show the in-plane electron velocities indicated by arrows on top of the magnetic field lines, with colors in $\boldsymbol{j}\cdot\boldsymbol{E}'$, $j_\parallel E_\parallel$, $(\boldsymbol{j}\times\boldsymbol{B})_x$, and $(\boldsymbol{j}\times\boldsymbol{B})_z$. Here $\boldsymbol{E}'=\boldsymbol{E}+\boldsymbol{V}_e\times\boldsymbol{B}$ is the electric field in the moving frame of the electron velocity $\boldsymbol{V}_e$. From Figure 1(d), one can find that there is intense energy dissipation ($\boldsymbol{j}\cdot\boldsymbol{E}'>0$) in the merging region at $x=\sim1690d_e$, while there is a noticeable energy dynamo ($\boldsymbol{j}\cdot\boldsymbol{E}'<0$) inside the secondary island. The $\boldsymbol{j}\cdot\boldsymbol{E}'$ of the three large islands are not localized in their central regions but are distributed in a region of high density and high j_y current density, for example, at $x=\sim600d_e$ and $x=\sim800d_e$. In the upper right corner of Figure 1(d), it is perhaps noteworthy that a spatially oscillatory energy conversion exists along the separatrix. In this study, we focus on the energy conversions located in the central region of the secondary island and the merging region at $x=\sim1690d_e$. From the close-up of the secondary island, as shown in Figure 1(h), one can see that the electrons are in circular motion inside the secondary island. Moreover, the in-plane Lorentz force ($\boldsymbol{j}\times\boldsymbol{B}$) is pointing toward the center of the island.

Figures 2(a)–(f) show the numerical data along a $z=0$ cut between $60d_e\leqslant x\leqslant120d_e$ the magnetic and electric fields ($\boldsymbol{B}$, $\boldsymbol{E}'$), the ion and electron plasma velocity and density ($\boldsymbol{V}_i$, $\boldsymbol{V}_e$, n_e), and the current density ($\boldsymbol{j}$) in the secondary island. At the center of the island, as marked by the vertical line, there is a small dip in the magnetic field strength associated with an increase in the plasma density. Figures 2(d) and (f) indicate that the strong axial current density j_y is carried by the electrons. To remove the numerical noise of the electron velocity and the electric field, a 2D Gaussian smoothing filter is implemented. Three dot products of $\boldsymbol{V}_e\cdot(\boldsymbol{j}\times\boldsymbol{B})=w_1$, $\boldsymbol{j}\cdot\boldsymbol{E}=w_2$, and $\boldsymbol{j}\cdot\boldsymbol{E}'=w_3$ are analyzed for energy conversion, where the quantity w_1 is the rate of work done by the Lorentz force on the electrons and $w_3=w_2-w_1$. As shown in Figure 2(d), the sign of the in-plane electron velocity V_{ez} is reversed during the crossing of the secondary island, indicating that the electrons are in circular motion around the secondary island, as shown in Figure 1(h). In Figure 2(g), the comparison of w_1 and w_2 shows that the pattern of w_1 exhibits a bipolar signature, which is different from that of w_2. It can be found that the reversal of the normal field B_z is aligned with that of w_1. The averages of w_1 and w_2 ($\langle w_1\rangle$ and

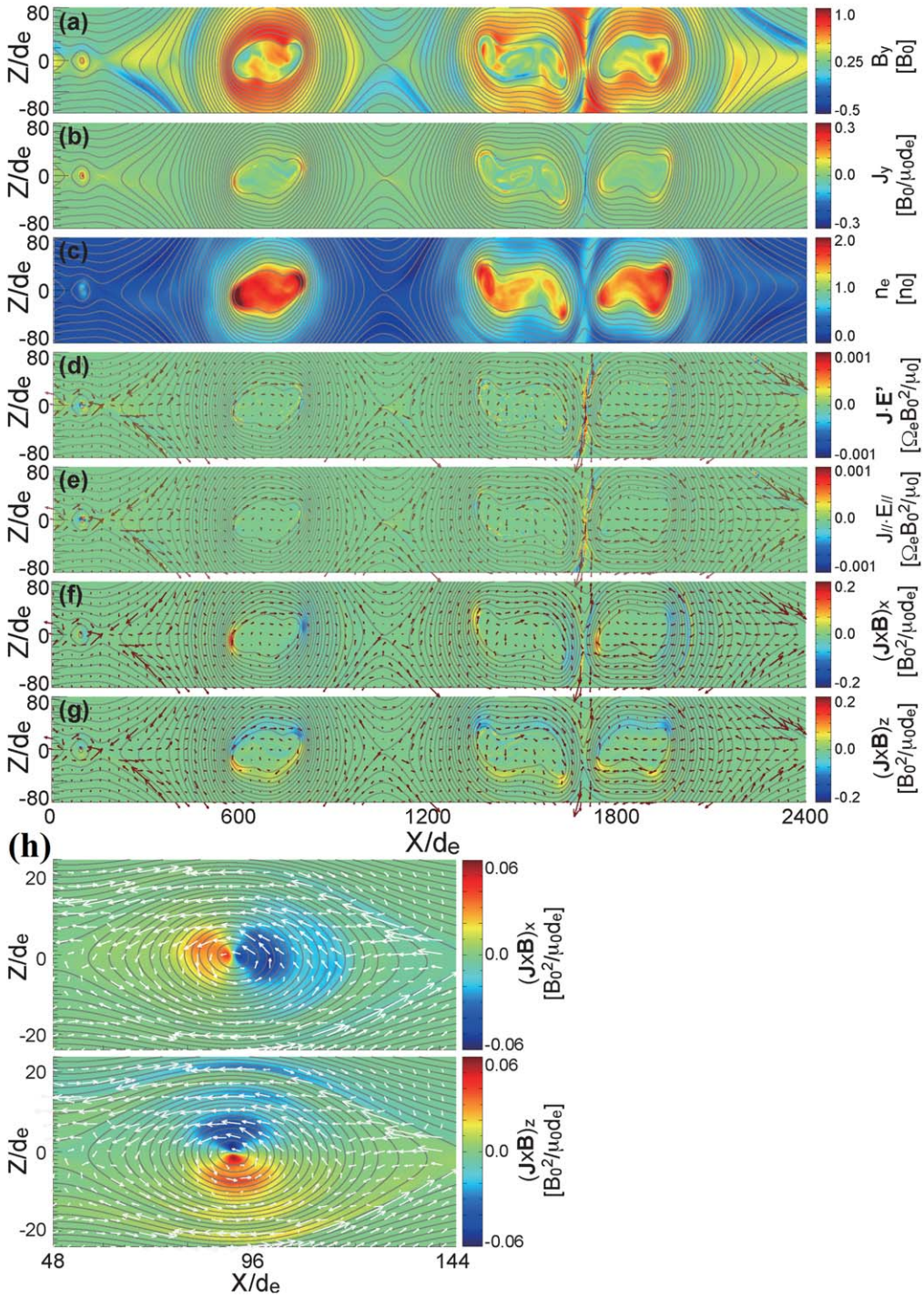

Figure 1. (a)–(c) Magnetic field maps in the x–z plane (the reconnection plane), with colors in the axial magnetic field B_y, the axial current density j_y, and the electron density, at the time $t = 90\ \Omega_i^{-1}$. (d)–(g) In-plane electron velocities denoted by arrows on top of the magnetic field lines, with colors in $\boldsymbol{j} \cdot \boldsymbol{E}'$, $j_{\parallel}E_{\parallel}$, $(\boldsymbol{j} \times \boldsymbol{B})_x$, and $(\boldsymbol{j} \times \boldsymbol{B})_z$. (h) Close-up of the in-plane electron velocity and magnetic field lines of the secondary island.

$(\langle w_2 \rangle)$ over $80d_e \leqslant x \leqslant 100d_e$ are -0.21×10^{-6} and -0.53×10^{-3}, respectively. Ideally, $(\langle w_1 \rangle$ is expected to be zero due to the bipolar pattern. The $|\langle w_1 \rangle|$ is ~2523 times smaller than $|\langle w_2 \rangle|$ because the electrons are in circular motion and the Lorentz force is pointing toward the center of the island, as shown in Figures 1(h), which is analogous to the centripetal force in a circular motion. Therefore, the average work done by the Lorentz force on the particles is negligible in a circular motion around the island. Note that the $(\langle w_1 \rangle$ is small at other z values within the secondary island (not shown) and that the circular motion of the particles is viewed from the guiding center perspective. The patterns of w_2 and w_3 in Figure 2(h) are similar to each other and there is a significant energy dynamo ($w_3 < 0$ and $\{w_3\}_{\min} = -0.22 \times 10^{-2}$) at the center of the secondary island, which has not been reported in either simulation or observational results. The $\{w_3\}_{\min}$ is the minimum of w_3 and corresponds to $\sim -2.5\ \mathrm{nWm}^{-3}$ for a reconnecting field $B_0 = 20$ nT. This magnitude is comparable to the energy conversion discovered in a magnetotail flux rope reported by Huang et al. (2019).

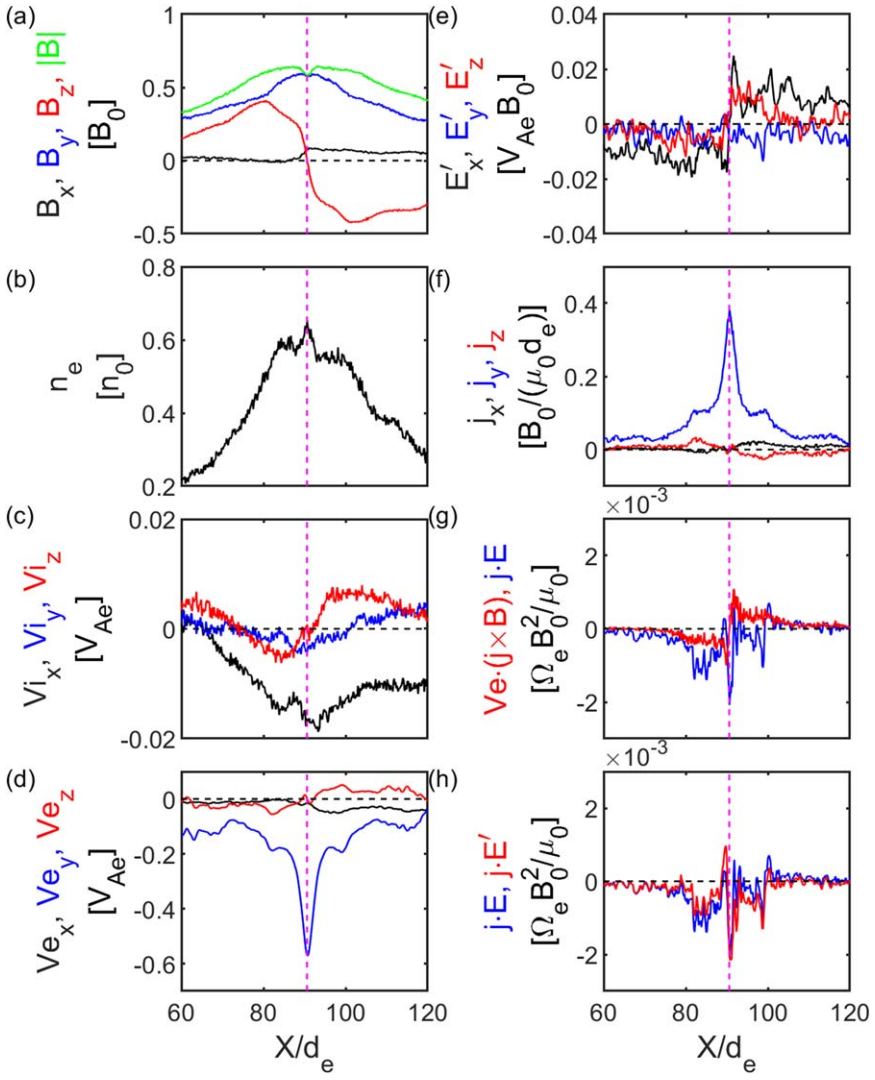

Figure 2. (a)–(f) Simulated data taken at the secondary island. (g)–(h) Comparisons of the rates of the energy conversions. The vertical line denotes the center of the island. The V_{Ae} is the electron Alfvén speed based on B_0 and n_0.

Figure 3 shows the numerical fields and plasma parameters along a $z = 0$ cut between $1660d_e \leqslant x \leqslant 1720d_e$ in the merging region between two coalescing islands, with the same format as Figure 2. In the figure, the vertical line denotes the merging point. In contrast to the secondary island, a significant decrease in the magnetic field strength accompanied by a decrease in density is seen in the merging region. There is a bifurcated current density in j_y and j_z, where the current density j_z is enhanced as compared to the one in the secondary island. These current densities are mainly carried by the electrons. The patterns of w_1 and w_2 are different, but similar between w_2 and w_3. A different type of energy conversion exists in this merging region with significant energy dissipation ($w_3 > 0$ and $\{w_3\}_{\max} = 0.22 \times 10^{-2}$). This intense dissipation in the merging region has previously been reported by simulation studies (e.g., Zenitani et al. 2011; Zhou et al. 2014) and MMS observations (e.g., Burch et al. 2016; Torbert et al. 2016; Webster et al. 2018) as well.

Figures 4(a) and 4(b) show the relationship between w_1 and w_2 and the relationships of w_3 with $j_{\parallel}E_{\parallel}$, $\boldsymbol{j}_{\perp} \cdot \boldsymbol{E}'_{\perp}$, and $E_{\parallel}$, along with the parallel and perpendicular components of electron temperature, current density, and $\boldsymbol{E}'$, for (a) the secondary island and (b) the merging region. The subscripts 1, 2, and 3 of $j_{\perp}$ and $E'_{\perp}$ denote the x, y, and z components. Note that the parallel direction near the island center or the X-line is pointed in the out-of-plane direction, for a finite guide field reconnection. As enclosed by the black vertical lines in Figures 4(a) and 4(b), the energy dynamo ($w_3 < 0$) and dissipation ($w_3 > 0$) are accompanied by the $j_{\parallel}$ and $T_{e\parallel}$ enhancement, where a low correlation between w_1 and w_2 is obtained for the secondary island ($cc_1 = -0.049$) and the merging region ($cc_1 = -0.417$). For the secondary island, the w_3 is highly correlated with $E_{\parallel}$ and $j_{\parallel}E_{\parallel}$ ($cc_2 = 0.887$ and $cc_3 = 0.976$), therefore a low correlation ($cc_4 = 0.613$) between $\boldsymbol{j}_{\perp} \cdot \boldsymbol{E}'_{\perp}$ and w_3 is obtained. Opposite results are seen in the merging region. The w_3 is weakly correlated with $E_{\parallel}$ and $j_{\parallel}E_{\parallel}$ ($cc_2 = 0.090$ and $cc_3 = 0.293$). As a result, a high correlation ($cc_4 = 0.897$) between $\boldsymbol{j}_{\perp} \cdot \boldsymbol{E}'_{\perp}$ and w_3 is obtained.

Figure 4(c) shows the analysis of the results of the energy conversion in the secondary island at $t = 105\ \Omega_i^{-1}$. A remarkable result is that the pattern of w_2 is now similar to w_1 but different than w_3, where a high correlation coefficient ($cc_1 = 0.977$) is obtained between w_1 and w_2. This is different from the previous results for the secondary island at $t = 90\ \Omega_i^{-1}$.

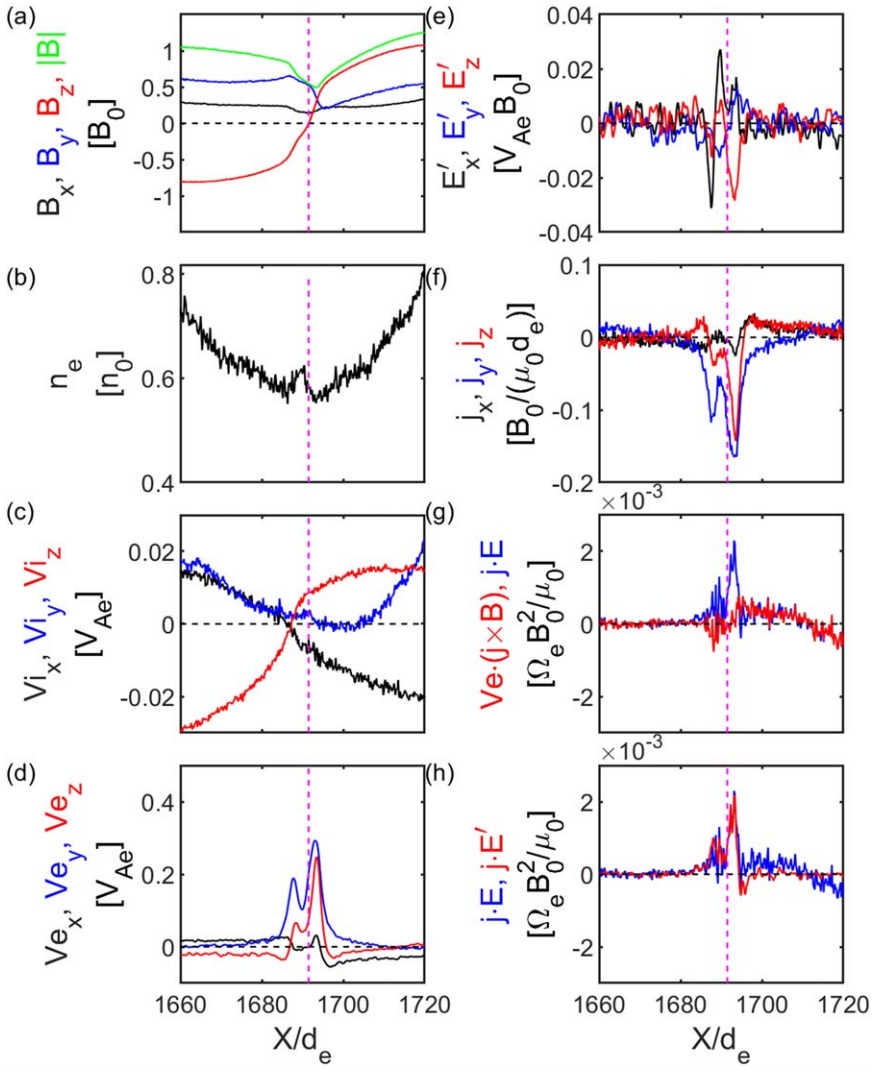

Figure 3. Simulated data and energy conversion results for the merging region between two coalescing islands, the same format as Figure 2. The vertical line denotes the merging point.

As enclosed by the black vertical lines, some results of Figures 4(a) and (c) are consistent; for example, the w_3 is highly correlated with $E_\parallel$ ($cc_2 = 0.903$) and $j_\parallel E_\parallel$ ($cc_3 = 0.930$). Note that the energy dynamo portion is dominated by $\boldsymbol{j}_\perp \cdot \boldsymbol{E}'_\perp$ at $t = 105\ \Omega_i^{-1}$.

3.2. Observational Results

In this section, three ion-scale magnetic islands observed by the MMS spacecraft are demonstrated to compare favorably with the simulation results. Two of them (FR1 and FR2) were observed in Earth's magnetopause (Teh et al. 2017) and the third one (FR3) was in the magnetotail (Teh et al. 2018). The diameters of FR1, FR2, and FR3 were ∼5, ∼11, ∼6 ion inertial lengths (∼236, ∼497, and ∼250 electron inertial lengths), respectively. The ratios of the reconnection guide field to the reconnecting field were ∼0.25 and ∼0.20 for the two reconnection events studied by Teh et al. (2017) and Teh et al. (2018), consistent with the one implemented in the simulation. Note that the magnetic islands studied by Teh et al. (2017) and Teh et al. (2017) were only separated by ∼8 minutes. The data were based on the MMS1 measurements of magnetic fields from the fluxgate magnetometer (FGM; Russell et al. 2016), electric fields from the electric double probes (EDP; Lindqvist et al. 2016), and electron and ion plasma moments from the fast plasma investigation (FPI; Pollock et al. 2016), with time resolutions in the burst modes. Vector components are shown in the LMN boundary coordinates. For FR1 and FR2, LMN axes in geocentric solar ecliptic (GSE) are $L = (0.210, -0.314, 0.926)$, $M = (-0.424, -0.882, -0.203)$, and $N = (0.881, -0.350, -0.318)$, where the $\boldsymbol{M}$ and $\boldsymbol{N}$ axes are the results of 10° rotation about the $\boldsymbol{L}$ axis in the LMN systems used by Teh et al. (2017). This 10° rotation aims to align the reversal of the normal magnetic field B_N with that of w_1 for FR1. For FR3, $\boldsymbol{L} = (0.998, -0.064, -0.028)$, $\boldsymbol{M} = (0.067, 0.990, 0.121)$, and $\boldsymbol{N} = (0.020, -0.123, 0.992)$, which are the same as those used by Teh et al. (2018).

Figures 5(a)–(h) show the observations and the energy conversion for FR1, with the same physical quantities shown in Figure 2, in the time interval 09:01:04–09:01:06 UT on 10 January 2016. The island is characterized by a bipolar B_N and the field strength enhancement at the center of the island as indicated by the magenta vertical line. The current density is calculated as $\boldsymbol{j} = qn_e(\boldsymbol{V}_i - \boldsymbol{V}_e)$ from the FPI data, which is mainly carried by the electrons. Here q is the electron charge. At the vertical line in Figures 5(d) and (g), the sign of the in-

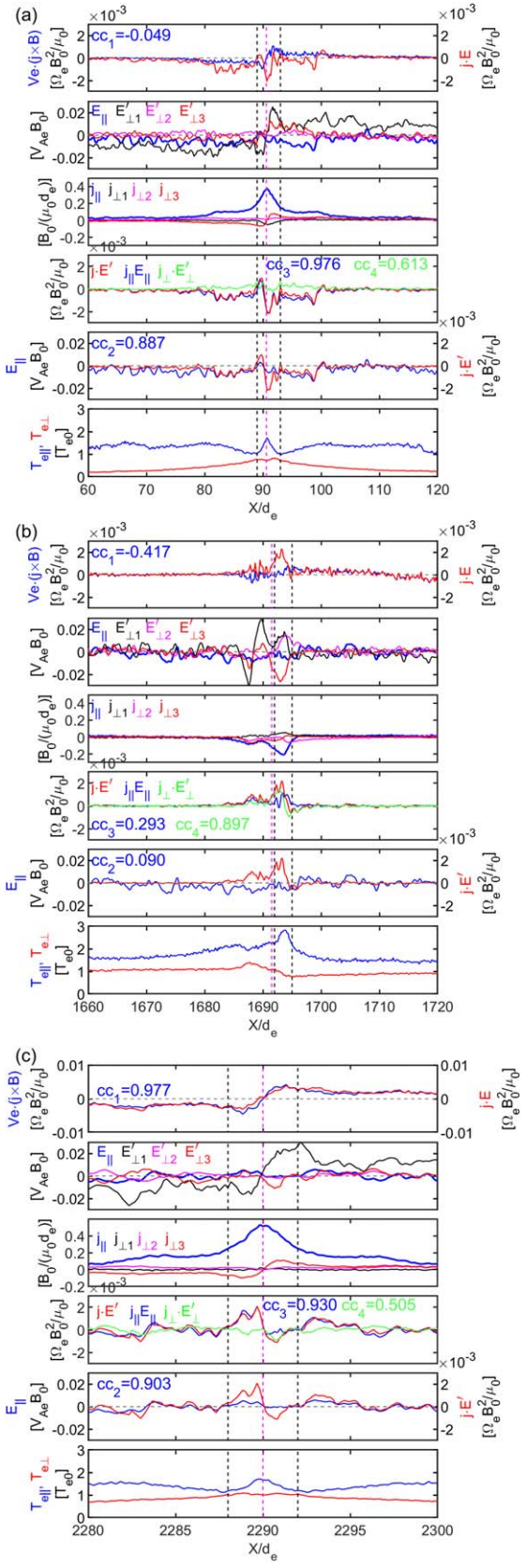

Figure 4. Results of the correlation analysis for (a) the secondary island and (b) the merging region at $t = 90\ \Omega_i^{-1}$. The magenta vertical line denotes (a) the center of the island and (b) the merging point. (c) The corresponding results for the secondary island at the later time $t = 105\ \Omega_i^{-1}$. The black vertical lines enclose the region where the $j_\parallel$ is enhanced. The subscripts 1, 2, and 3 denote the x, y, and z components.

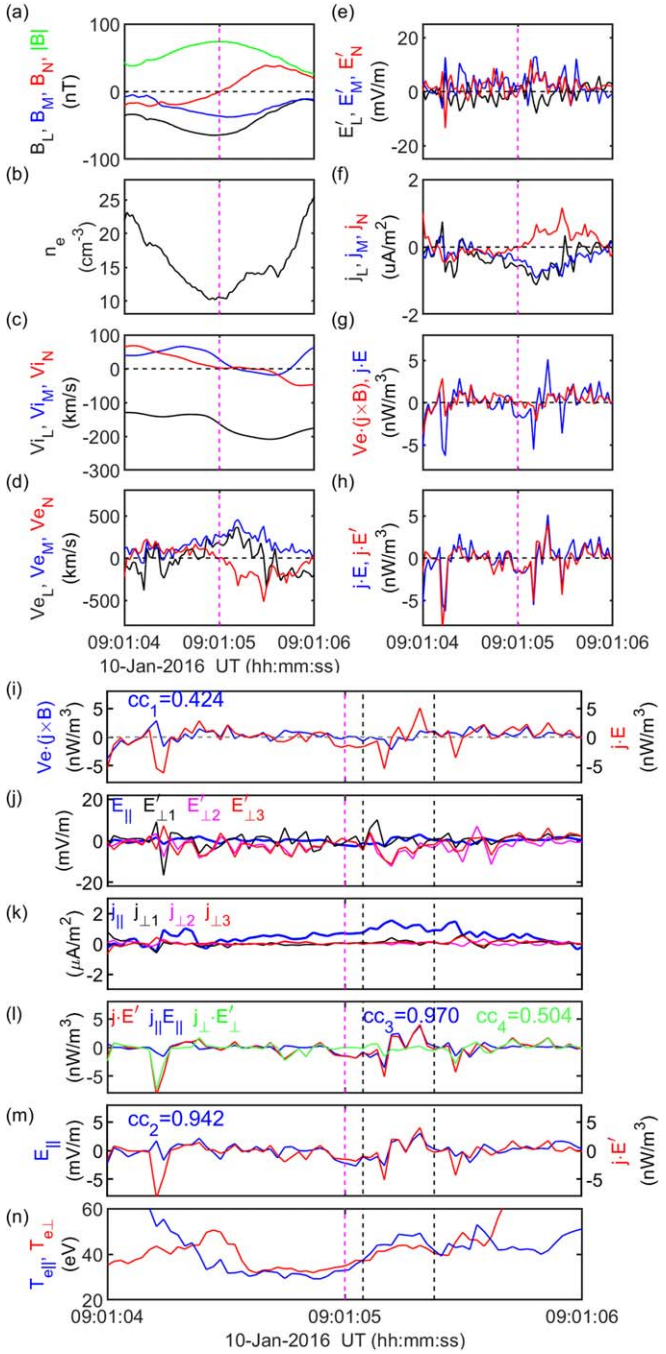

Figure 5. (a)–(h) MMS1 measurements of FR1 and the comparisons of the rates of energy conversion; the same physical quantities shown in Figure 2. The magenta vertical line denotes the center of the island. (i)–(n) Results of the correlation analysis, the same format as Figure 4(a). The interval enclosed by the black vertical lines is used for correlation analysis.

plane velocity V_{eN} is reversed and a bipolar pattern is seen for w_1. Figures 5(i)–(n) show the same physical quantities as Figure 4(a). As enclosed by the black vertical lines, both the energy dynamo and dissipation are observed, where the temperature $T_{e\parallel}$ is increased. The peak magnitudes of the energy dynamo and dissipation are comparable. The correlation results are $cc_1 = 0.424$, $cc_2 = 0.942$, $cc_3 = 0.970$, and $cc_4 = 0.504$. The high correlation cc_2 and cc_3 are consistent with the simulation results shown in Figure 4(a) for the secondary island, for which the energy conversion resulted

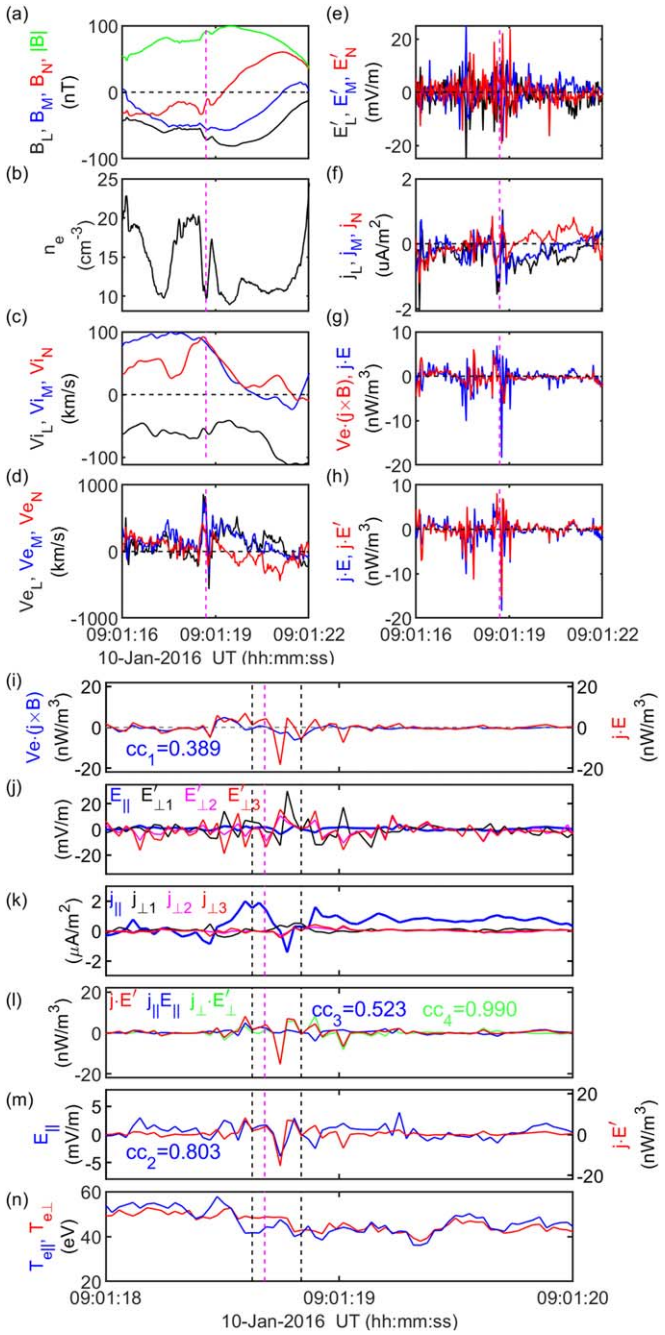

Figure 6. MMS1 observations and analysis of the results for FR2, the same format as Figure 5.

from $j_{\parallel}E_{\parallel}$. In addition, a stronger energy dynamo due to $\boldsymbol{j}_{\perp} \cdot \boldsymbol{E}'_{\perp}$ is found near the edge of the island, as shown in Figure 5(l) at ∼09:01:04.2 UT. This was obtained in the simulation at a later time (see Figure 4(c)), but not in Figure 4(a).

Figure 6 shows the observations and the analysis of the results for FR2, with the same format as Figure 5, in the time interval 09:01:16–09:01:22 UT on 10 January 2016. Note that Figures 6(i)–(n) are shown for the time interval 09:01:18–09:01:20 UT. Figures 6(d) and 6(f) indicate that the current density is mainly carried by the electrons. At the vertical line in Figures 6(d) and 6(g), the signs of V_{eL} and V_{eN} are reversed and a bipolar pattern is present for w_1. It can be seen in Figure 6(a) that the reversal of B_N at the vertical line is not at the zero crossing. This offset can be adjusted by rotating 21° about the $\boldsymbol{L}$ axis from Teh et al. (2017). Since the results of w_1, w_2, and w_3 and associated correlation results are independent of the boundary coordinates, the LMN systems of FR1 are therefore used for FR2. In contrast to the island center, the density in the island is increased with decreasing the magnetic field strength, as shown in Figure 6(b). This density increase has been interpreted as the consequence of the magnetosheath plasma feeding into the island along the magnetic field lines (Teh et al. 2017). As enclosed by the black vertical lines, a strong energy dynamo is seen, where the temperature $T_{e\parallel}$ is slightly increased. The correlation results are $cc_1 = 0.389$, $cc_2 = 0.803$, $cc_3 = 0.523$, and $cc_4 = 0.990$. The energy dynamo resulted from $\boldsymbol{j}_{\perp} \cdot \boldsymbol{E}'_{\perp}$, although there is a high correlation ($cc_2 = 0.803$) between $E_{\parallel}$ and w_3, as shown in Figure 6(m).

Figure 7 shows the observations and the analysis of the results for FR3, with the same format as Figure 5, in the time interval 22:35:06–22:35:14 UT on 11 July 2017. Note that Figures 7(i)–(n) are shown for the time interval 22:35:07–22:35:10 UT. At the magenta vertical line in Figures 7(d), (g), and (i), where B_N reverses sign, the signs of the in-plane electron velocity are not reversed and therefore no bipolar pattern is found for w_1. As enclosed by the black vertical lines, the energy conversion resulted from $\boldsymbol{j}_{\perp} \cdot \boldsymbol{E}'_{\perp}$, where the correlation results are $cc_1 = 0.291$, $cc_2 = 0.391$, $cc_3 = 0.395$, and $cc_4 = 0.980$. In contrast to the FR2 event, FR3 displays a low correlation ($cc_2 = 0.391$) between $E_{\parallel}$ and w_3.

4. Summary and Discussion

A two-dimensional fully kinetic simulation of multiple island coalescence with a small reconnection guide field has been examined to analyze the energy conversion for the secondary island and the merging region between two coalescing islands. The dot product of $\boldsymbol{V}_e \cdot (\boldsymbol{j} \times \boldsymbol{B}) = w_1$ was introduced into the energy conversion analysis to compare with $\boldsymbol{j} \cdot \boldsymbol{E} = w_2$. The key simulation results are summarized as follows: (1) significant energy dynamo ($\boldsymbol{j} \cdot \boldsymbol{E}' < 0$) due to $j_{\parallel}E_{\parallel}$ is reported for the first time inside a secondary island in the simulation, where the parallel electric field $E_{\parallel}$ and $\boldsymbol{j} \cdot \boldsymbol{E}'$ are highly correlated; (2) significant energy dissipation ($\boldsymbol{j} \cdot \boldsymbol{E}' > 0$) resulted from $\boldsymbol{j}_{\perp} \cdot \boldsymbol{E}'_{\perp}$ is found in the merging region; (3) both types of energy conversions are accompanied by enhancements in $j_{\parallel}$ and $T_{e\parallel}$; (4) the bipolar pattern of w_1 is an indicator that the electrons are circulating in the island; (5) the pattern of w_2 may reflect the bipolar pattern of w_1 within the secondary island in a given phase of its evolution and that similarity between w_1 and w_2 depends on the evolution as shown in Figures 4(a) and 4(c). Three ion-scale magnetic islands (FR1, FR2, and FR3) observed by the MMS spacecraft were presented. Although the energy conversion processes of the island involved in the real situation are more complex, consistent results are achieved for FR1 and the simulated secondary island, in terms of the bipolar pattern of w_1, the high correlation cc_2 and cc_3, and the $j_{\parallel}$ and $T_{e\parallel}$ enhancement. In contrast, a different type of energy conversion is found across FR2 and FR3, where the $\boldsymbol{j}_{\perp} \cdot \boldsymbol{E}'_{\perp}$ is dominant in the energy dynamo and dissipation.

The high correlation ($cc_2 = 0.803$) between $E_{\parallel}$ and w_3 found at FR2 is a surprising result because the energy dynamo resulted from $\boldsymbol{j}_{\perp} \cdot \boldsymbol{E}'_{\perp}$. This would lead to the misunderstanding that the $j_{\parallel}E_{\parallel}$ is dominant in the energy conversion, if only looking at the correlation cc_2. The reason for this result is

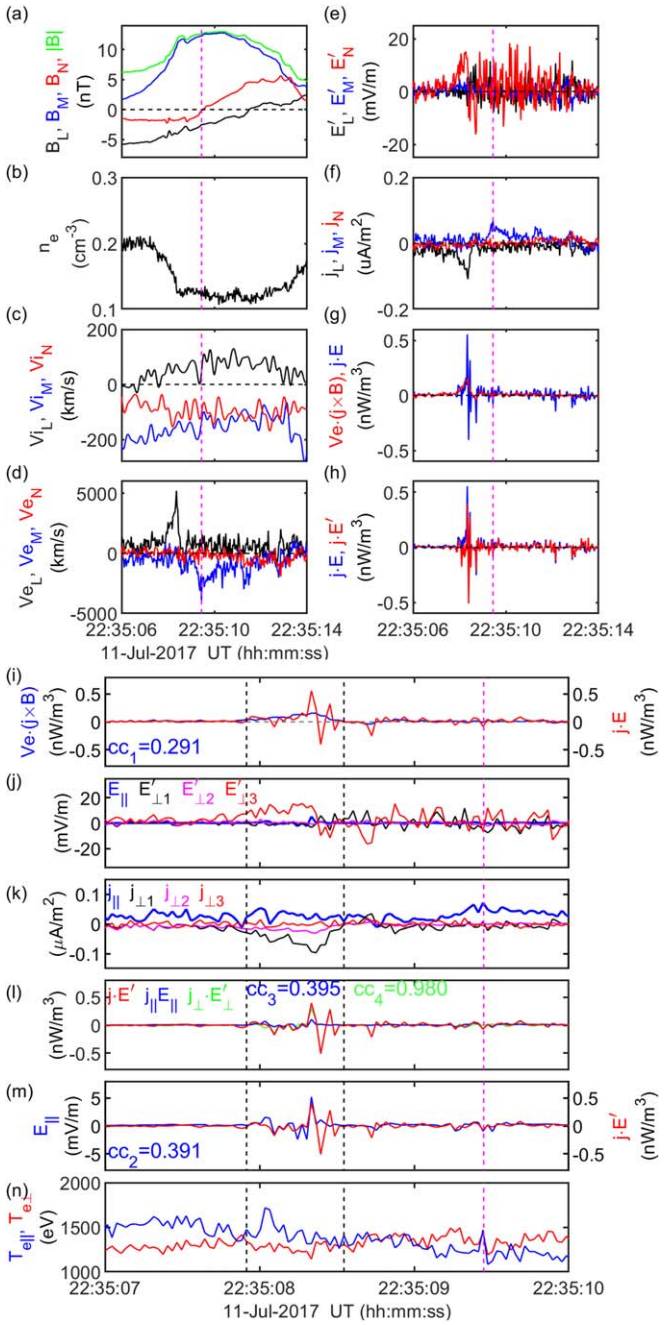

Figure 7. MMS1 observations and analysis results for FR3, the same format as Figure 5.

unclear yet. The high correlation ($cc_1 = 0.977$) between w_1 and w_2, as seen in Figure 4(c), is an interesting result. Previous simulation studies by Egedal et al. (2009) revealed that the electrons become trapped when a sign reversal happens in the $E_\parallel$. This sign reversal of $E_\parallel$ can be seen in the interval enclosed by the black vertical lines in Figure 4(c). One may suggest that the circulating particles could be trapped inside the island under this circumstance. To address this issue will be the future research task.

This work was supported by the grant of Universiti Kebangsaan Malaysia (GP-2020-K020730). Work at the Space Research Institute was funded by Austrian Research Fund (FWF) (P32175-N27). This research was also carried out by the international joint research program of the Institute for Space-Earth Environmental Research (ISEE), Nagoya University. Many thanks to PRACE for awarding T.K.M. Nakamura access to MareNostrum at Barcelona Supercomputing Center (BSC), Spain. Special thanks to the dedicated efforts of the entire MMS mission team for data access. MMS data can be downloaded through the NASA CDAWeb at http://cdaweb.gsfc.nasa.gov/.

ORCID iDs

W.-L. Teh https://orcid.org/0000-0002-7114-1543
T. K. M. Nakamura https://orcid.org/0000-0003-4550-2947
S. Zenitani https://orcid.org/0000-0002-0945-1815
T. Umeda https://orcid.org/0000-0001-6882-9200
R. Nakamura https://orcid.org/0000-0002-2620-9211

References

Bowers, K. J., Albright, B. J., Yin, L., Bergen, B., & Kwan, T. J. T. 2008, PhPl, 15, 055703
Bowers, K. J., Albright, B. J., Yin, L., et al. 2009, JPhCS, 180, 012055
Burch, J. L., Torbert, R. B., Phan, T. D., et al. 2016, Sci, 352, aaf2939
Chen, L.-J., Bhattacharjee, A., Puhl-Quinn, P. A., et al. 2008, NatPh, 4, 19
Chen, Z. Z., Fu, H. S., Wang, Z., et al. 2021, GeoRL, 48, e89722
Dahlin, J. T., Drake, J. F., & Swisdak, M. 2017, PhPl, 24, 092110
Daughton, W., Scudder, J., & Karimabadi, H. 2006, PhPl, 13, 072101
Drake, J. F., Swisdak, M., Che, H., & Shay, M. A. 2006, Natur, 443, 553
Eastwood, J. P., Phan, T.-D., Mozer, F. S., et al. 2007, JGRA, 112, A06235
Egedal, J., Daughton, W., Drake, J. F., Katz, N., & Le, A. 2009, PhPl, 16, 050701
Hoshino, M. 2005, JGRA, 110, A10215
Hoshino, M., Mukai, T., Terasawa, T., & Shinohara, I. 2001, JGRA, 106, 25979
Huang, S. Y., Jiang, K., Yuan, Z. G., et al. 2019, GeoRL, 46, 580
Huang, S. Y., Vaivads, A., Khotyaintsev, Y. V., et al. 2012, GeoRL, 39, L11103
Khabarova, O., Zank, G. P., Li, G., et al. 2015, ApJ, 808, 181
Le Roux, J. A., Webb, G. M., Khabarova, O. V., Zhao, L.-L., & Adhikari, L. 2019, ApJ, 887, 77
Le Roux, J. A., Zank, G. P., & Khabarova, O. V. 2018, ApJ, 864, 158
Lindqvist, P.-A., Olsson, G., Torbert, R. B., et al. 2016, SSRv, 199, 137
Lu, S., Artemyev, A. V., Angelopoulos, V., & Pritchett, P. L. 2020, ApJ, 896, 105
Nakamura, T. K. M., Genestreti, K. J., Liu, Y.-H., et al. 2018, JGRA, 123, 9150
Nakamura, T. K. M., Stawarz, J. E., Hasegawa, H., et al. 2020, JGRA, 125, e27515
Nakamura, T. K. M., Teh, W.-L., Zenitani, S., et al. 2023, PhPl, 30, 022902
Oka, M., Fujimoto, M., Shinohara, I., & Phan, T. D. 2010b, JGRA, 115, 8223
Oka, M., Phan, T.-D., Krucker, S., Fujimoto, M., & Shinohara, I. 2010a, ApJ, 714, 915
Pollock, C., Moore, T., Jacques, A., et al. 2016, SSRv, 199, 331
Pritchett, P. L. 2008, PhPl, 15, 102105
Russell, C. T., Anderson, B. J., Baumjohann, W., et al. 2016, SSRv, 199, 189
Song, H.-Q., Chen, Y., Li, G., Kong, X.-L., & Feng, S.-W. 2012, PhRvX, 2, 021015
Stawarz, J. E., Eastwood, J. P., Genestreti, K. J., et al. 2018, GeoRL, 45, 8783
Tanaka, K. G., Yumura, T., Fujimoto, M., et al. 2010, PhPl, 17, 102902
Teh, W.-L. 2022a, ApJ, 930, 22
Teh, W.-L. 2022b, ApJ, 934, 181
Teh, W.-L., Denton, R. E., Sonnerup, B. U. Ö., & Pollock, C. 2017, GeoRL, 44, 6517
Teh, W.-L., Eriksson, S., Sonnerup, B. U. Ö., et al. 2010, GeoRL, 37, L21102
Teh, W.-L., Nakamura, R., Karimabadi, H., Baumjohann, W., & Zhang, T. L. 2014, JGRA, 119, 2933
Teh, W.-L., Nakamura, T. K. M., Nakamura, R., et al. 2017, JGRA, 122, 2040
Teh, W.-L., Nakamura, T. K. M., Nakamura, R., & Umeda, T. 2018, JGRA, 123, 8122
Torbert, R. B., Burch, J. L., Giles, B. L., et al. 2016, GeoRL, 43, 5918
Wang, R. S., Lu, Q. M., Du, A. M., & Wang, S. 2010, PhRvL, 104, 175003
Wang, R. S., Lu, Q. M., Nakamura, R., et al. 2016, NatPh, 12, 263W
Webster, J. M., Burch, J. L., Reiff, P. H., et al. 2018, JGRA, 123, 4858W

Zank, G. P., le Roux, J. A., Webb, G. M., Dosch, A., & Khabarova, O. 2014, ApJ, 797, 28Z
Zenitani, S., Hesse, M., Klimas, A., & Kuznetsova, M. 2011, PhRvL, 106, 195003
Zenitani, S., Shinohara, I., & Nagai, T. 2012, GeoRL, 39, L11102
Zhao, L.-L., Zank, G. P., Chen, Y., et al. 2019, ApJ, 872, 4
Zhao, L.-L., Zank, G. P., Khabarova, O., et al. 2018, ApJL, 864, L34
Zhao, Y., Wang, R. S., Lu, Q. M., et al. 2016, JGRA, 121, 10898
Zhong, Z. H., Zhou, M., Tang, R. X., et al. 2020, GeoRL, 47, e85141
Zhou, M., Berchem, J., Walker, R. J., et al. 2017, PhRvL, 119, 055101
Zhou, M., Pang, Y., Deng, X. H., Huang, S. Y., & Lai, X. S. 2014, JGRA, 119, 6177Z